# Supplementary information

**Table of Contents**

**1. Sample bias dependent STM images of G/FL-CrI₃/Gr**



a Z: $V_S$ = -2V, 1 nm
b Z: $V_S$ = -1.5V
c Z: $V_S$ = -1.2V
d Z: $V_S$ = -1V
e Z: $V_S$ = -0.5V
f Z: $V_S$ = 0.1V
g Z: $V_S$ = 0.3V
h Z: $V_S$ = 0.4V
i Z: $V_S$ = 0.5V
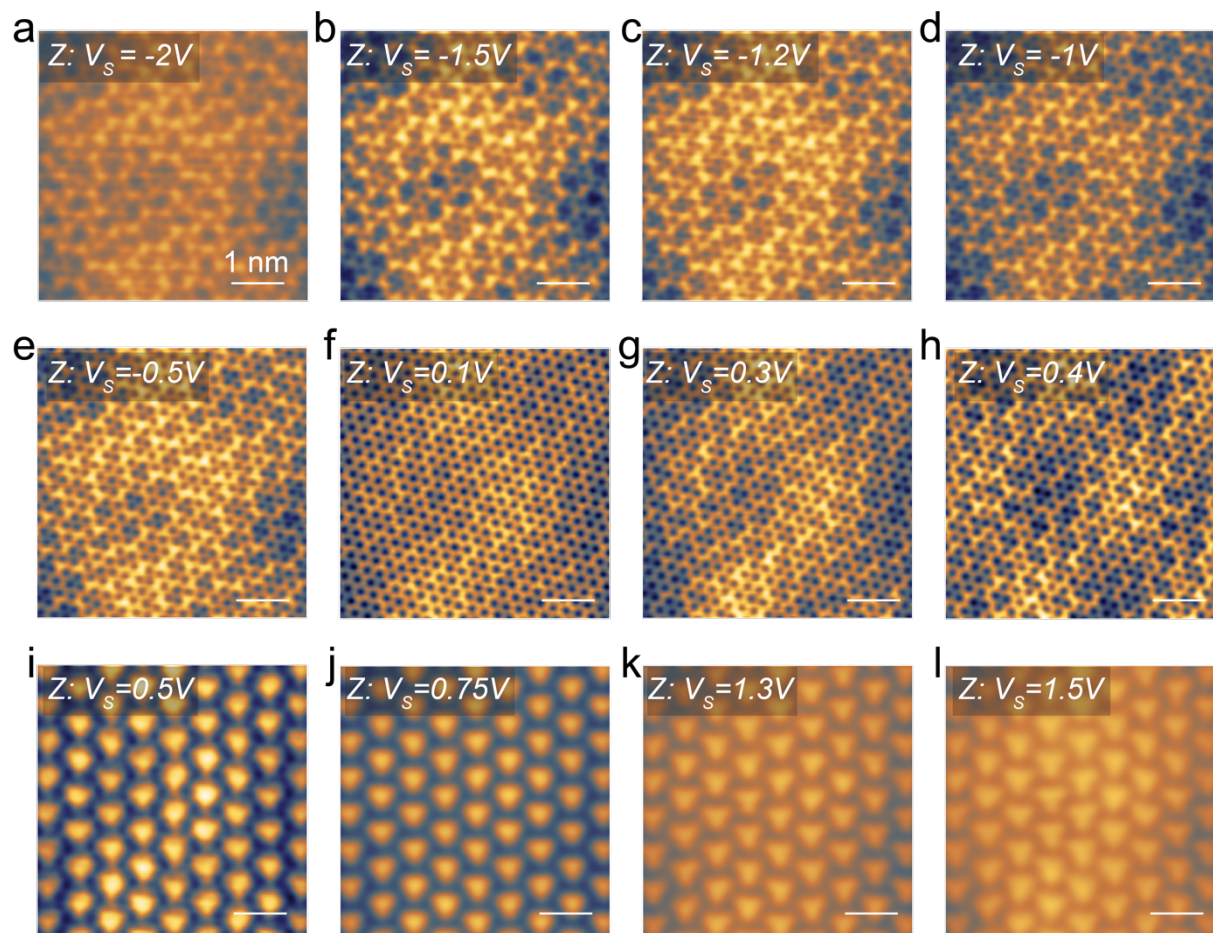j Z: $V_S$ = 0.75V
k Z: $V_S$ = 1.3V
l Z: $V_S$ = 1.5V

**Figure S1**. **Sample bias dependent STM images of the G/FL-CrI₃/Gr.** The tunneling current is 1 nA for all STM images.
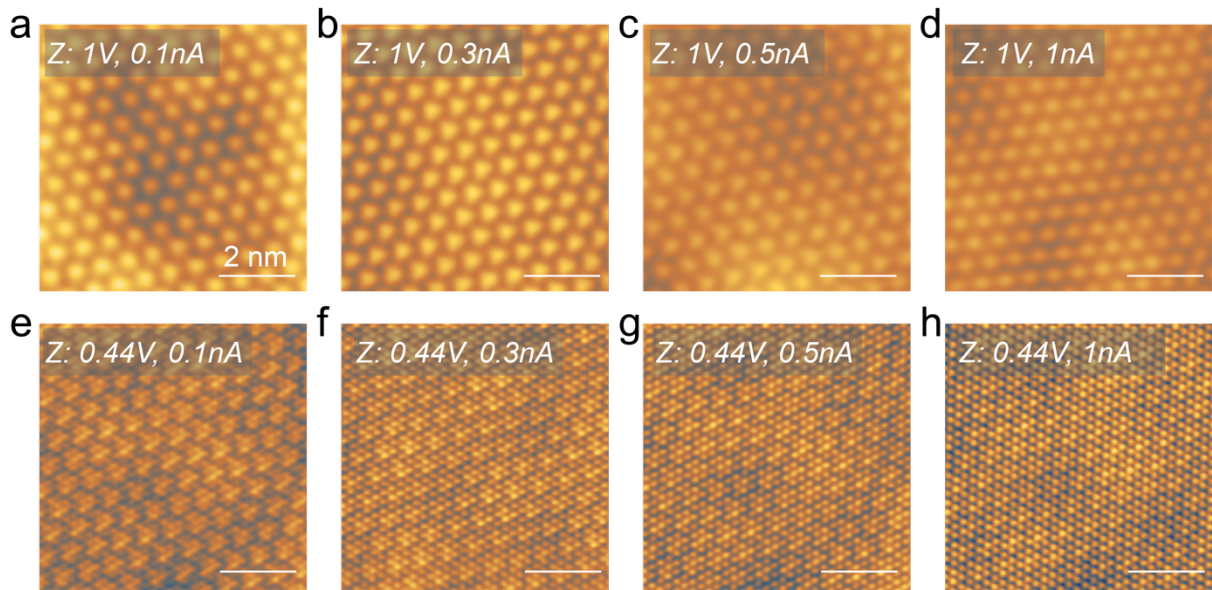
**Figure S2. STM images of the G/FL-CrI₃/Gr recorded at varied tunneling current.** (a-d) STM images ($V_s = 1$ V) recorded at varied tunneling current from 0.1 nA to 1 nA.Note the STM images could be taken on different areas. All these STM images resolves $CrI_3$ lattice, independent of tunnelling current. That is because the electronic states probed are deep into the $CrI_3$ conduction band and thus the $CrI_3$ states have a major contribution to the tunneling current. (e-h) STM images ($V_s = 0.44V$) recorded at varied tunneling current from 0.1nA to 1nA. A smaller positive bias ($V_s = 0.44V$) probes the electronic states near the $CrI_3$ conduction band edge as well as graphene states. In this case, the weight of integrated graphene states and integrated $CrI_3$ states may be comparable so that both graphene lattice and $CrI_3$ lattice can be resolved. A variation of tunneling current from 0.1 nA to 1 nA have a limited influence on the visualization of graphene lattice. An increase of tunneling current makes the graphene ($CrI_3$) lattice slightly more (less) prominent.
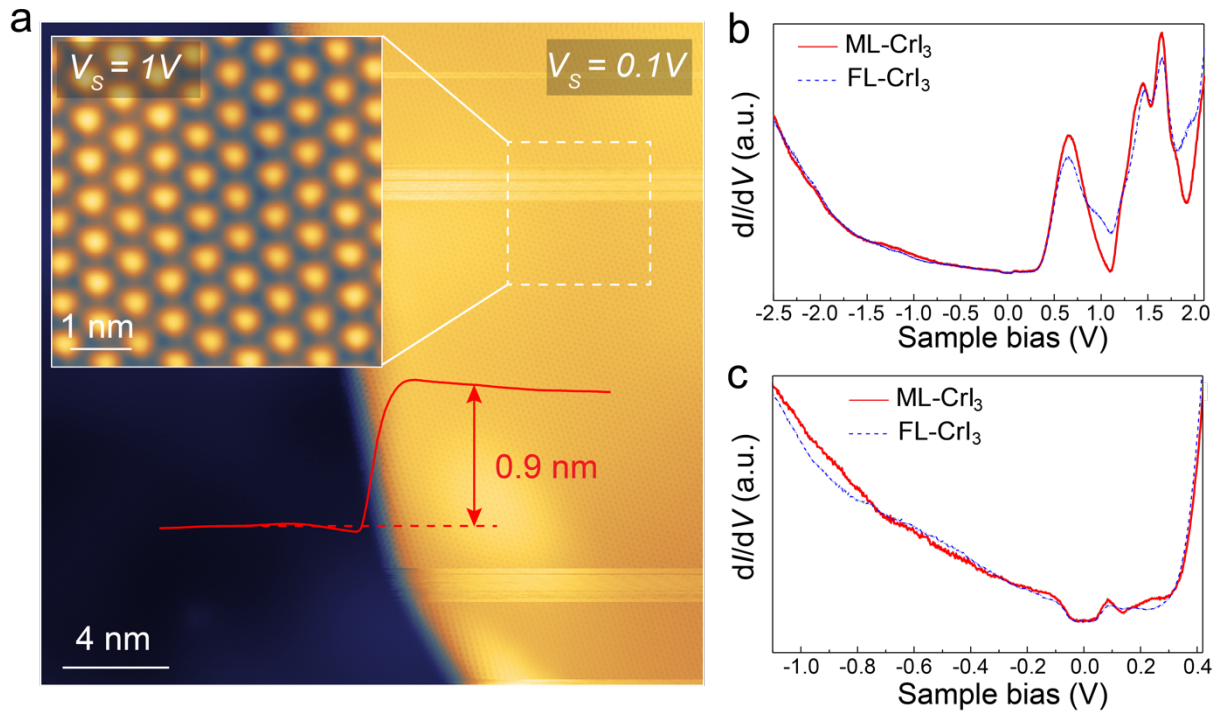
## 2. The STM images and STS spectra of G/ML-CrI$_3$/Gr



**Figure S3**. **The STM images and STS spectra of G/ML-CrI$_3$/Gr.** (a) STM image of G/ML-CrI$_3$/Gr ($V_s = 0.1$ V, $I_t = 0.8$ nA). The inset: a zoom-in STM image of the selected area (marked by dash square, $V_s = 1$ V, $I_t = 0.1$ nA) shows the CrI$_3$ lattice. The bottom graphite flake covered by graphene appears as the dark region on the left side of (a), while graphene covered monolayer CrI$_3$ appears as the bright region on the right side of (a). The line profile (red line) reveals a single-layer step with an apparent height of ~0.9 nm. (b) The d$I$/d$V$ spectrum of G/ML-CrI$_3$/Gr (red solid line) taken in a large sample bias window ($-2.5$ V $\leq V_s \leq 2.1$ V), compared with the d$I$/d$V$ spectrum of G/FL-CrI$_3$/Gr (blue dashed line). (c) The d$I$/d$V$ spectrum of G/ML-CrI$_3$/Gr (red solid line) taken in a small sample bias window ($-1.2$ V $\leq V_s \leq 0.42$ V), compared with the d$I$/d$V$ spectrum of G/FL-CrI$_3$/Gr (blue dashed line).

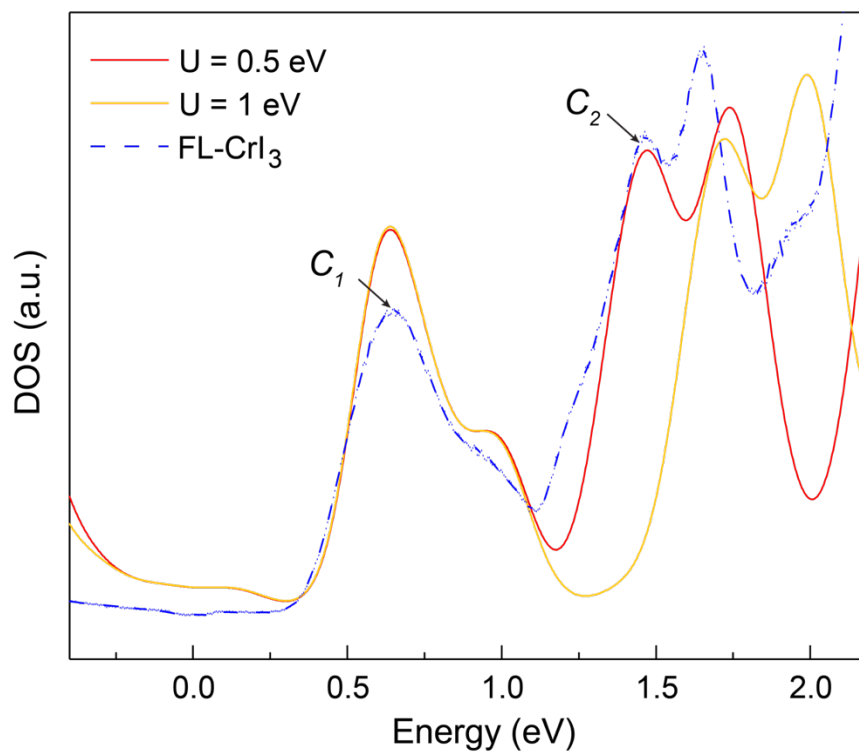**3. Calculated DOS of G/ML-CrI$_3$ with different Hubbard U**



**Figure S4**. **Calculated DOS of G/ML-CrI$_3$ with a Hubbard U of 0.5 eV (solid red line) and 1 eV (solid yellow line) compared with the d$I$/d$V$ spectrum of G/FL-CrI$_3$/Gr (dashed blue line).** Note, the calculated DOS of G/ML-CrI$_3$ is manually offset by 0.55 eV to align with the energy position of $C_1$ states resolved in d$I$/d$V$ spectrum.

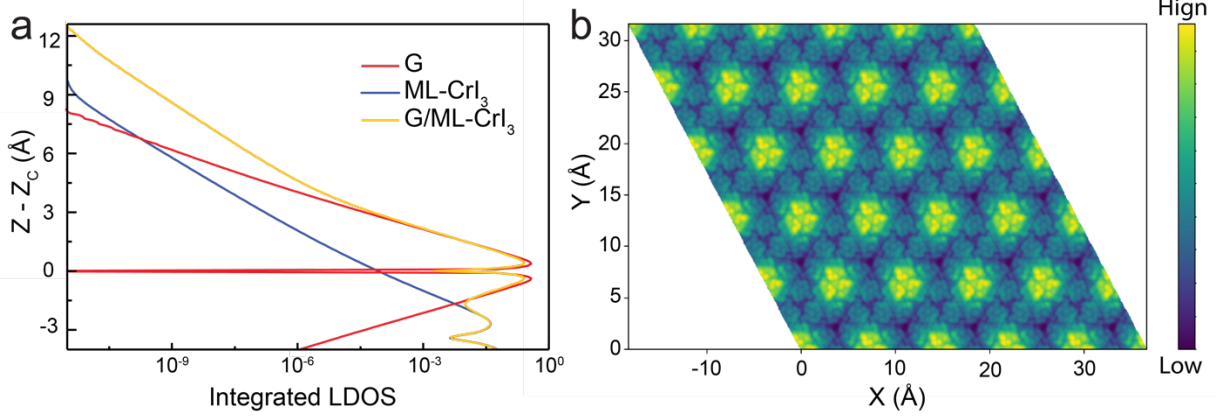## 4. The transparency of graphene to tunneling electrons



**Figure S5**. **The transparency of graphene to tunneling electrons.** (a) Integrated LDOS from $E_F$ to $E - E_F = 3$ eV for the isolated graphene, ML-CrI$_3$, and the hybrid G/ML-CrI$_3$ as a function of vertical distance. All vertical distances are referenced to the graphene plane ($Z - Z_c = 0$ Å). (b) Simulated STM image of G/ML-CrI$_3$ acquired at a vertical distance of $Z - Z_c = 6$ Å and $V_s = 3$ V.

With a few assumptions, the LDOS decays exponentially as a function of tip-sample distance z[1]:

$$LDOS\ (z) = C \cdot e^{-z/\lambda}$$

where C is a constant, $\lambda$ is the decay length. The inverse decay length can be written as $\lambda^{-1} = 2\sqrt{\frac{2m\phi}{\hbar^2} + k_{\parallel}^2}$, which is determined by the work function $\phi$ and the in-plane wave vector of the states $k_{\parallel}$.

Here we have calculated the vertical decay of the integrated LDOS from $E_F$ to $E - E_F = 3$ eV for the isolated graphene, ML-CrI$_3$, and the hybrid G/ML-CrI$_3$ heterostructure with a separation of 3.5 Å between graphene and CrI$_3$ surface. The isolated ML-CrI$_3$ is vertically offset to align with the CrI$_3$ in the G/ML-CrI$_3$ heterostructure. As shown in Figure S5a, the

graphene states undergo a much faster decay than ML-CrI$_3$ states with a crossover at 7 Å above graphene. It indicates graphene states have a small decay length which can be attributed to the large in-plane wave vector $k_{\parallel}$ of graphene states[2]. Moreover, the vertical decay of integrated LDOS of the G/ML-CrI$_3$ hybrid system sets apart from that of graphene at the distance above 4 Å. When the vertical distance is larger than 4 Å ($Z - Z_c > 4$ Å), the effective decay length of the G/ML-CrI$_3$ system is nearly identical to the decay length of ML-CrI$_3$, which suggests that the integrated LDOS of G/ML-CrI$_3$ has a dominant contribution from the underlying ML-CrI$_3$. This is consistent with the feature (CrI$_3$ lattice) observed in the simulated STM image of G/ML-CrI$_3$ at $Z - Z_c = 6$ Å and $V_s = 3$ V (Figure S5b).

**5. The moiré superlattice of G/FL-CrI$_3$/Gr at a twist angle $\varphi = 16°$**
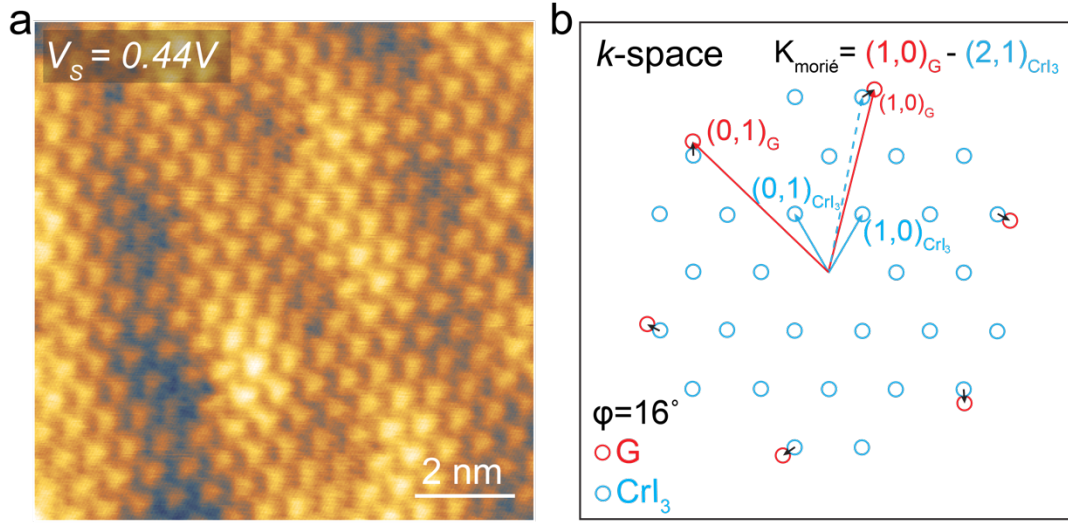


**Figure S6. The moiré superlattice of G/FL-CrI$_3$/Gr at a twist angle $\varphi = 16°$ between graphene and FL-CrI$_3$.** (a) STM image ($V_s = 0.44$ V, $I_t = 0.3$ nA) in the same area of Figure 4a. (b) The reciprocal lattice of graphene (red circle) and CrI$_3$ (blue circle) at a twist angle $\varphi = 16°$.

We performed the geometrical analysis of the moiré superlattice in G/FL-CrI$_3$/Gr. A combination of Figure S6a and Figure 4a reveals a twist angle of $\varphi = 16°$ between the graphene and FL-CrI$_3$. We are able to extract the periodicity and orientation of the moiré superlattice of G/FL-CrI$_3$ based on this twist angle, in good agreement with the experimental results.

It is noted the that reciprocal lattice vector of moiré pattern ($\vec{K}_{morié}$) can be regarded as the difference between the reciprocal lattice vector of graphene and CrI$_3$[3]. Figure S6b shows the reciprocal lattice vectors of graphene and FL-CrI$_3$ indexed by vectors $(r, s)_G$ and $(m, n)_{CrI_3}$. As shown in Figure S6b, the $(1,0)_G$- and $(2,1)_{CrI_3}$- spot almost overlap in $k$-space. The difference of two vectors leads to the reciprocal lattice vector of a possible moiré pattern as symmetrically equivalent to: $\vec{K}_{morié} = (1,0)_G - (2,1)_{CrI_3}$. As a result, $\vec{K}_{morié}$ leads to a moiré superlattice in real space where the moiré length is $|M_1| = |M_2| = 3.18$ nm and the

rotation angle between graphene and moiré superlattice is $\theta = 41°$. Meanwhile, we experimentally determine the periodicity and orientation of moiré superlattice from STM image (Figure 4a). The moiré length is measured to be $|M_1|' = |M_2|' = 3.14 \pm 0.01$ nm. The angle between graphene and moiré superlattice is measured to be $\theta' = 41°$. The simulated results are in good agreement with our experimental observation.

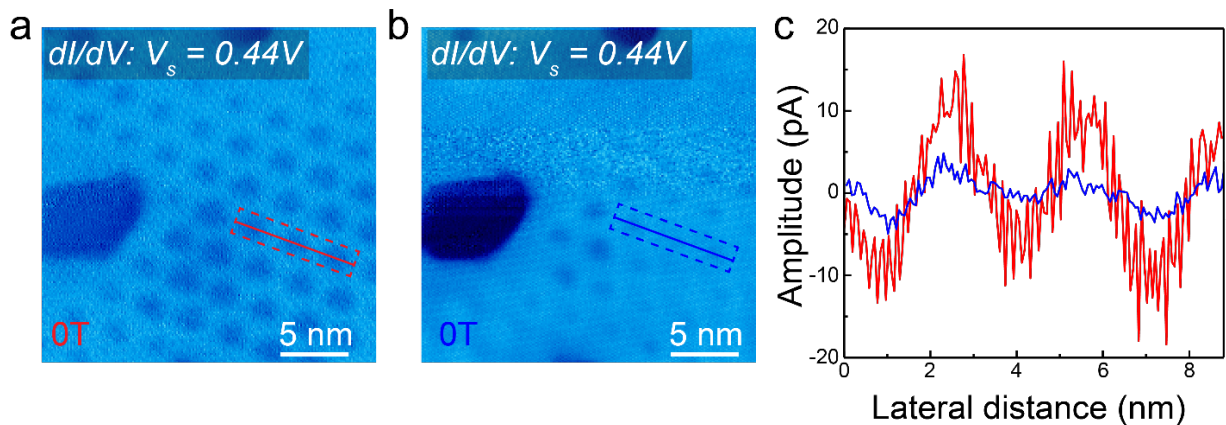## 6. The magnetic field dependent d$I$/d$V$ maps of G/FL-CrI$_3$/Gr



**Figure S7. The amplitude of moiré contrast in the d$I$/d$V$ maps of G/FL-CrI$_3$/Gr ($V_s$ = 0.44 V, $I_t$ = 0.5 nA).** (a) The d$I$/d$V$ map taken at the initial stage ($\mu_0 H = 0$ T) before ramping up the magnetic field. (b) The d$I$/d$V$ map taken at the final stage ($\mu_0 H = 0$ T) after ramping down the magnetic field. (c) The line profiles across the indicated areas in the d$I$/d$V$ maps. The difference between the maximum and minimum d$I$/d$V$ signal is defined as the amplitude of moiré contrast, which is measured to be ~20 pA in image (a) and reduced to ~ 6 pA in image (b).
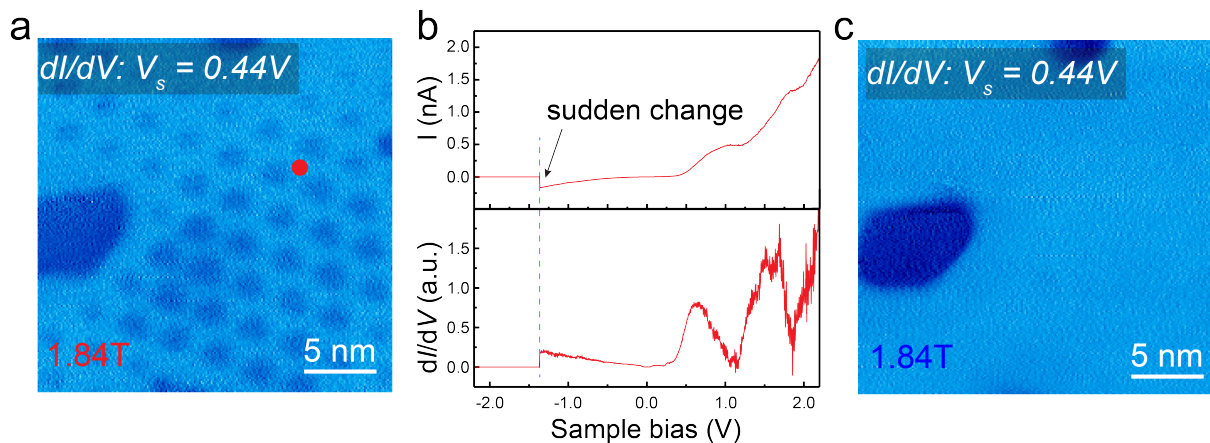


**Figure S8. AFM-FM magnetic phase transition induced by the magnetic field with the assistance of tip-induced local gating.** (a) The d$I$/d$V$ map ($V_s$ = 0.44 V, $I_t$ = 0.5 nA) upon the application of 1.84 T magnetic field. We then took point d$I$/d$V$ spectroscopy (the tip position is indicated by the red dot). (b) A sudden change of the $I$-$V$ and d$I$/d$V$ signal. (c) The d$I$/d$V$ map ($V_s$ = 0.44 V, $I_t$ = 0.5 nA) taken after the sudden change of the d$I$/d$V$ signal. The sudden change of $I$-$V$ and d$I$/d$V$ signal is likely to be associated with an abrupt AFM-FM magnetic phase transition induced by the magnetic field with the assistance of tip-induced local gating.

This can be attributed to the magneto-electric effect and the influence of doping on magnetization reported in previous studies[4-6].
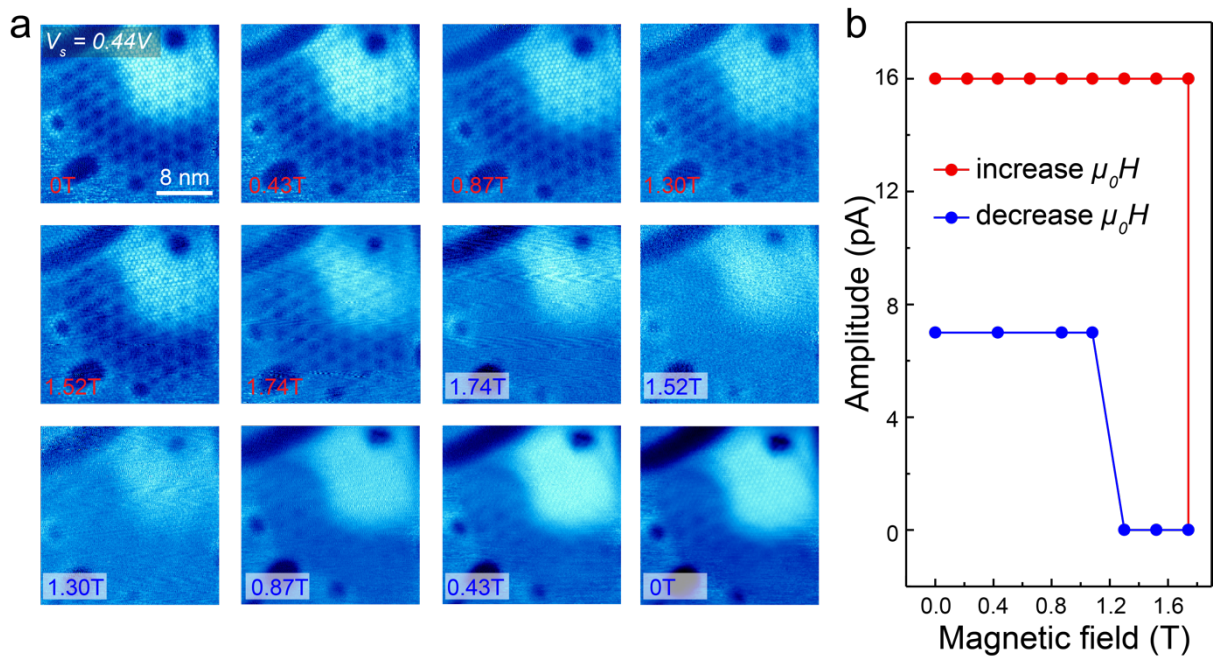


**Figure S9. Magnetic field dependent moiré contrast in d$I$/d$V$ maps.** (a) Another set of magnetic field dependent d$I$/d$V$ maps of G/FL-CrI$_3$/Gr ($V_s$ = 0.44 V, $I_t$ = 0.5 nA). The critical field was 1.74 T when moiré contrast disappeared. (b) Magnetic field dependent moiré contrast in the d$I$/d$V$ maps taken at $V_s$ = 0.44 V and $I_t$ = 0.5 nA.
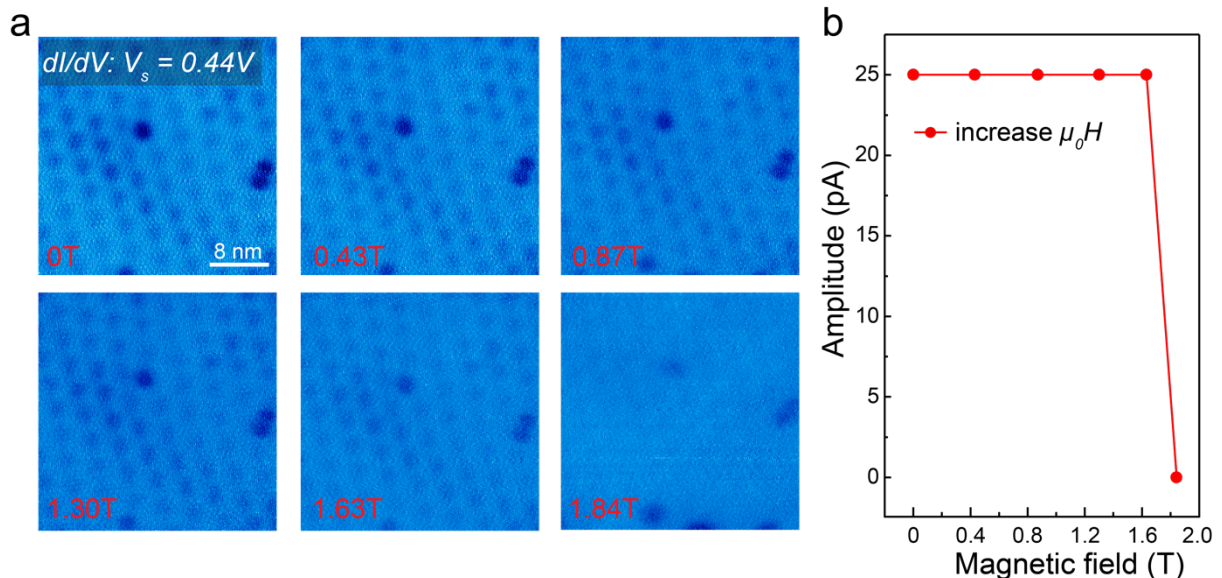


**Figure S10. Moiré contrast in the d$I$/d$V$ map vanished right after applying a magnetic field of 1.84 T in certain sample regions.** (a) Magnetic field dependent d$I$/d$V$ maps of G/FL-CrI$_3$/Gr ($V_s$ = 0.44 V, $I_t$ = 1 nA). (b) Magnetic field dependent moiré contrast in the d$I$/d$V$ maps ($V_s$ = 0.44 V, $I_t$ = 1 nA).

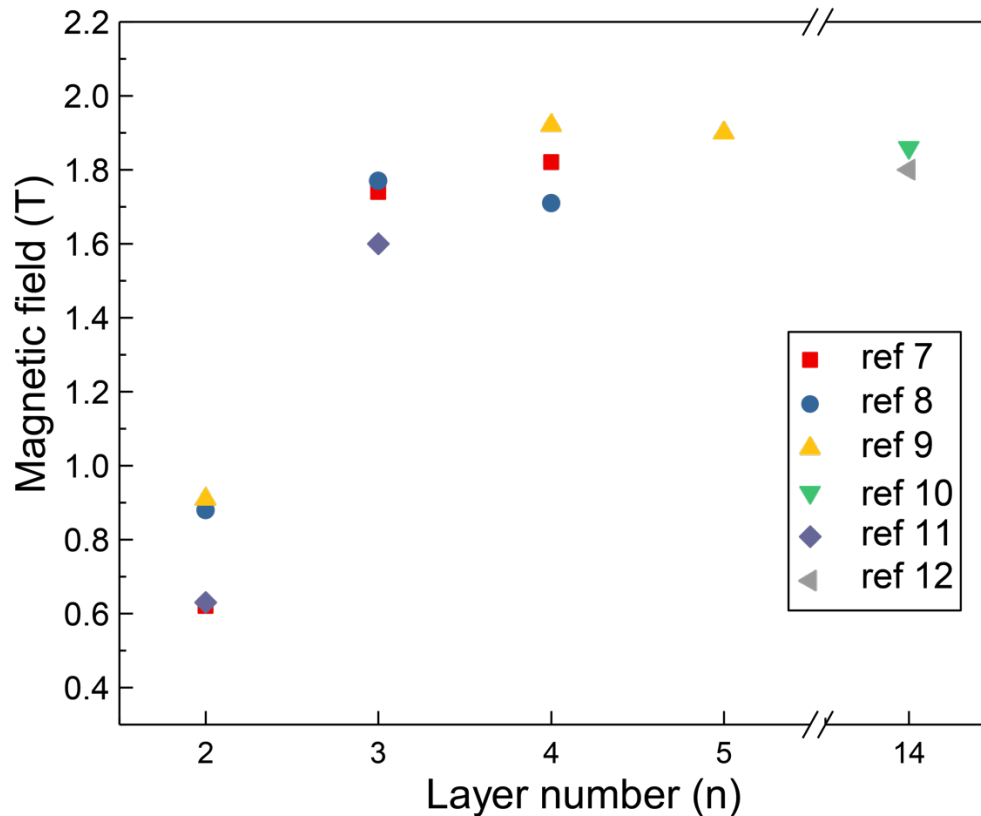**7. The reported magnetic field for AFM-FM transition in FL-CrI$_3$**



**Figure S11. The typical magnetic field for AFM-FM transition on FL-CrI$_3$ in the previous reports[7-12].** The critical magnetic field for AFM-FM transition in thin CrI$_3$ flakes (layer number $n > 2$) is reported to be ranged from 1.60 T to 1.92 T (average value of $1.79 \pm 0.10$ T). The variation of the critical magnetic field is likely due to the sample-to-sample difference, the formation of domain structures and the influence of local environment[4,13,14]. Unfortunately, 1.84 T is the upper limit of the magnetic field in our system, which may be insufficient to flip the spin in certain sample regions. In such a case, AFM-FM phase transition could be triggered with the assistance of tip-induced local gating during d$I$/d$V$ spectroscopic measurement, as illustrated in Figure S8. In addition, in the certain region of sample, we also observed that moiré contrast vanished in the d$I$/d$V$ map immediately at a magnetic field of 1.84 T as shown in Figure S10.

**8. The atomic registry dependent electronic structures of G/four-layer CrI₃**
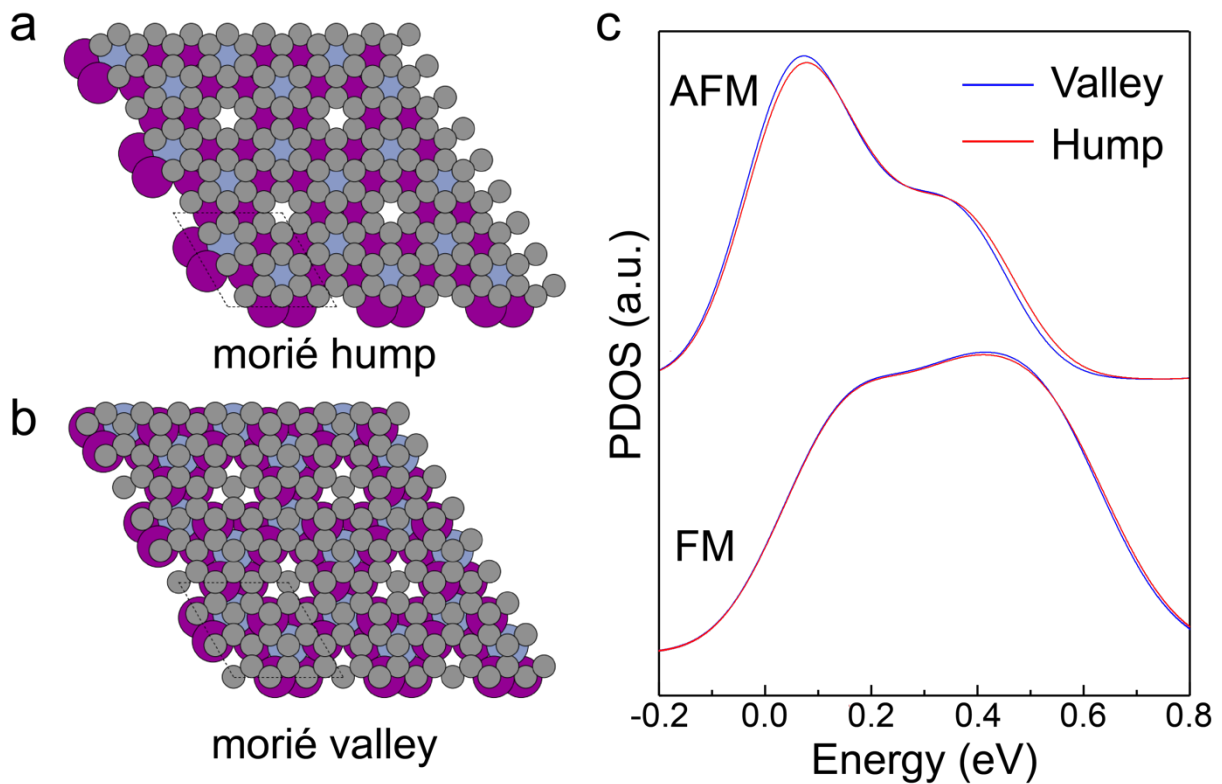


**Figure S12. The atomic registry dependent electronic structures of G/four-layer CrI₃.** (a) The atomic model of moiré hump. (b) The atomic model of moiré valley. (c) Calculated PDOS of top CrI₃ layer in moiré valley (blue) and moiré hump (red) when four-layer CrI₃ are AFM-coupled and FM-coupled.

A direct simulation of the large moiré superlattice of G/FL-CrI₃ at a twist angle $\varphi = 16°$ is computationally costly, beyond the capability of our computation power. To qualitatively demonstrate the atomic registry dependent electronic structure of G/FL-CrI₃ by DFT calculations, we use a $(3 \times 3)$ supercell of graphene placed on a single unit cell of four-layer CrI₃ with different atomic arrangements to mimic the local atomic registry in moiré hump and moiré valley separately (Figure S12a-b). Figure S12c compares the PDOS of top CrI₃ layer in moiré valley and moiré hump under different magnetic order. Specifically, when the four-layer CrI₃ is interlayer AFM-coupled, there is a small but noticeable difference between PDOS

in the moiré hump and valley. By contrast, PDOS of top $CrI_3$ layer are nearly same in moiré hump and valley when four-layer $CrI_3$ are interlayer FM-coupled.

## 9. Method for theoretical calculation

The DFT calculations were performed with the electronic structure software package GPAW[15,16] using the projector augmented wave method and a plane wave basis. The LDA+U functional was used in the Dudarev approach[17] with a value of U=0.5 eV for the Cr $d$-orbitals. The value of U was chosen in order to reproduce the distance between the $C_1$ and $C_2$ peaks obtained from STS. Unless otherwise specified, for all calculations we considered a single unit cell of $CrI_3$ with ($3 \times 3$) unit cells of graphene adsorbed. The $CrI_3$ layers were stretched by 7% in order to obtain a lattice match with the LDA-optimized ($3 \times 3$) graphene unit cell. In all calculations, we employed a $12 \times 12$ Monkhorst-Pack grid of k-points, a Fermi smearing of 1 meV and a planewave cutoff of 600 eV. The structures were relaxed until all forces were less than 0.01 eV/Å. We considered the two adsorption geometries shown in Figure S12a-b. The graphene sheet shows a slightly stronger binding to $CrI_3$ in the hump geometry compared to that in the valley geometry. The binding energy difference between the two geometries is determined to be approximately 1 meV per C atom. All band structures, wavefunctions and projected density of states were performed with a non-selfconsistent inclusion of spin-orbit coupling[18].

The simulated STS and STM images were carried out with a modified Tersoff-Hamann approach[1] with the local density of stated (LDOS) being obtained as

$$LDOS(\boldsymbol{r}) = \sum_{nk} f_{nk} |\psi_{nk}(x, y, x)|^2 \delta(\varepsilon_{nk} - eV_{bias}) e^{-\alpha w_{nk}},$$

where $\varepsilon_{nk}$ is eigenenergy of the state $\psi_{nk}$, $f_{nk}$ are the occupation numbers and

$$w_{nk} = \sum_{ia} \left| \langle \psi_{nk} | \varphi_i^{C,a} \rangle \right|^2$$

is the total weight of the state $\psi_{nk}$ on the graphene sheet (the state $\varphi_i^{C,a}$ is atomic orbital $i$ on

carbon atom $a$). Thus the graphene states can be projected out of the LDOS by choosing a

finite value of $\alpha$.

**Reference:**

1      Tersoff, J. & Hamann, D. R. Theory and application for the scanning tunneling microscope. *Phys. Rev. Lett.* **50**, 1998 (1983).

2      González-Herrero, H. c. et al. Graphene tunable transparency to tunneling electrons: a direct tool to measure the local coupling. *ACS Nano* **10**, 5131-5144 (2016).

3      Zeller, P. & Günther, S. What are the possible moiré patterns of graphene on hexagonally packed surfaces? Universal solution for hexagonal coincidence lattices, derived by a geometric construction. *New J. Phys.* 16, 083028 (2014).

4      Jiang, S., Shan, J. & Mak, K. F. Electric-field switching of two-dimensional van der Waals magnets. *Nat. Mater.* **17**, 406-410 (2018).

5      Jiang, S., Li, L., Wang, Z., Mak, K. F. & Shan, J. Controlling magnetism in 2D CrI$_3$ by electrostatic doping. *Nat. Nanotech.* **13**, 549-553 (2018).

6      Jiang, S., Li, L., Wang, Z., Shan, J. & Mak, K. F. Spin tunnel field-effect transistors based on two-dimensional van der Waals heterostructures. *Nat. Electron.* **2**, 159-163 (2019).

7      Song, T. et al. Giant tunneling magnetoresistance in spin-filter van der Waals heterostructures. *Science* **360**, 1214-1218 (2018).

8      Klein, D. R. et al. Probing magnetism in 2D van der Waals crystalline insulators via electron tunneling. *Science* **360**, 1218-1222 (2018).

9      Li, T. et al. Pressure-controlled interlayer magnetism in atomically thin CrI$_3$. *Nat. Mater.* **18**, 1303-1308 (2019).

10      Zhong, D. et al. Van der Waals engineering of ferromagnetic semiconductor heterostructures for spin and valleytronics. *Sci. Adv.* **3**, e1603113 (2017).

11      Song, T. et al. Switching 2D magnetic states via pressure tuning of layer stacking. *Nat. Mater.* **18**, 1-5 (2019).

12    Wang, Z. et al. Very large tunneling magnetoresistance in layered magnetic semiconductor CrI$_3$. *Nat. Commun.* **9**, 1-8 (2018).

13    Huang, B. et al. Layer-dependent ferromagnetism in a van der Waals crystal down to the monolayer limit. *Nature* **546**, 270-273 (2017).

14    Thiel, L. et al. Probing magnetism in 2D materials at the nanoscale with single-spin microscopy. *Science* **364**, 973-976 (2019).

15    Enkovaara, J. e. et al. Electronic structure calculations with GPAW: a real-space implementation of the projector augmented-wave method. *J. Phys. Condens. Matter.* **22**, 253202 (2010).

16    Larsen, A. H. et al. The atomic simulation environment—a Python library for working with atoms. *J. Phys. Condens. Matter.* **29**, 273002 (2017).

17    Mosey, N. J. & Carter, E. A. Ab initio evaluation of Coulomb and exchange parameters for DFT+ U calculations. *Phys. Rev. B* **76**, 155123 (2007).

18    Olsen, T. Designing in-plane heterostructures of quantum spin Hall insulators from first principles: 1T′− MoS$_2$ with adsorbates. *Phys. Rev. B* **94**, 235106 (2016).